ADVANCED MATERIALS
www.advmat.de

Graphene Oxide-Supported Microwell Grids for Preparing Cryo-EM Samples with Controlled Ice Thickness

Min-Ho Kang, Junsun Park, Sungsu Kang, Sungho Jeon, Minyoung Lee, Ji-Yeon Shim, Jeeyoung Lee, Tae Jin Jeon, Min Kyung Ahn, Sung Mi Lee, Ohkyung Kwon, Byung Hyo Kim, Joel R. Meyerson, Min Jae Lee, Kwang-Il Lim, Soung-Hun Roh,* Won Chul Lee,* and Jungwon Park**

Cryogenic-electron microscopy (cryo-EM) is the preferred method to determine 3D structures of proteins and to study diverse material systems that intrinsically have radiation or air sensitivity. Current cryo-EM sample preparation methods provide limited control over the sample quality, which limits the efficiency and high throughput of 3D structure analysis. This is partly because it is difficult to control the thickness of the vitreous ice that embeds specimens, in the range of nanoscale, depending on the size and type of materials of interest. Thus, there is a need for fine regulation of the thickness of vitreous ice to deliver consistent high signal-to-noise ratios for low-contrast biological specimens. Herein, an advanced silicon-chip-based device is developed which has a regular array of micropatterned holes with a graphene oxide (GO) window on freestanding silicon nitride (Si_xN_y). Accurately regulated depths of micropatterned holes enable precise control of vitreous ice thickness. Furthermore, GO window with affinity for biomolecules can facilitate concentration of the sample molecules at a higher level. Incorporation of micropatterned chips with a GO window enhances cryo-EM imaging for various nanoscale biological samples including human immunodeficiency viral particles, groEL tetradecamers, apoferritin octahedral, aldolase homotetramer complexes, and tau filaments, as well as inorganic materials.

1. Introduction

Cryogenic-electron microscopy (cryo-EM) has become the preferred method to determine the 3D structures of proteins because it allows direct observation of protein structures without laborious and time-consuming steps to prepare and crystallize protein molecules.[1] In addition, cryo-EM is increasingly used to resolve conformational dynamics of protein molecules, including the effect of drug binding.[2] The method works by loading thin samples of frozen protein into a liquid-nitrogen-cooled transmission electron microscope, acquiring images using a high speed electron detector, and then processing these images using computational algorithms to generate a 3D structure.[3] To prepare samples for cryo-EM imaging, a droplet of protein solution is dispensed on a holey carbon support "grid," and then a specialized robot uses blotting paper to remove excess protein solution before plunging the grid into a coolant such as liquid ethane. The result is a thin (10–100 nm) layer of vitreous ice with the proteins or target molecules embedded inside. Ideally, the protein molecules adopt a range of orientations within the ice, and are suspended across holes in the carbon support film. These imaging holes range from a few hundred nanometers to a few micrometers in diameter.[4] 3D structures of important proteins, interactions between drug molecules and ion channel proteins,[5]

M.-H. Kang, S. Kang, M. Lee, J. Park
School of Chemical and Biological Engineering, and
Institute of Chemical Processes (ICP)
Seoul National University
Seoul 08826, Republic of Korea
E-mail: jungwonpark@snu.ac.kr

M.-H. Kang, S. Kang, M. Lee, J. Park
Center for Nanoparticle Research
Institute of Basic Science (IBS)
Seoul 08826, Republic of Korea

J. Park, S.-H. Roh
School of Biological Sciences
Seoul National University
Seoul 08826, Republic of Korea
E-mail: shroh@snu.ac.kr

The ORCID identification number(s) for the author(s) of this article can be found under https://doi.org/10.1002/adma.202102991.

DOI: 10.1002/adma.202102991

S. Jeon, W. C. Lee
Department of Mechanical Engineering
BK21FOUR ERICA-ACE Center
Hanyang University
Ansan, Gyeonggi 15588, Republic of Korea
E-mail: wonchullee@hanyang.ac.kr

J.-Y. Shim, K.-I. Lim
Department of Chemical and Biological Engineering
Sookmyung Women's University
Seoul 04310, Republic of Korea
E-mail: klim@sookmyung.ac.kr

J. Lee, M. J. Lee
Department of Biochemistry and Molecular Biology
Seoul National University College of Medicine
Seoul 03080, Republic of Korea

T. J. Jeon, O. Kwon
National Instrumentation Center for Environmental Management
Seoul National University
Seoul 08826, Republic of Korea

and the envelope proteins of pathogenic viruses such as severe acute respiratory syndrome coronavirus-2 (SARS-CoV-2) that causes COVID-19[6] have been extensively investigated with this technology.In addition, the great advancement of cryo-EM equipment and techniques has extended its applications to material science.[7] Structures of materials having radiation or air sensitivity and requiring analysis in a native aqueous state can be investigated using cryo-EM.[8]

Despite the great success of cryo-EM in exploring the structures of nanoscale entities, the cryo-EM sample preparation procedure lacks tight control over ice thickness, which is a dominant determinant in image quality and thus achievable structural resolution. Extensive sample screening is typically required to identify a "good" sample grid from a batch of samples, which hampers efficiency and the ability to fully exploit automated procedures for high-throughput 3D structure analysis.[9] Improvements in the reliability and reproducibility of cryo-EM sample preparation would enhance the utilization of cryo-EM in the basic sciences and commercial drug discovery. Cryo-EM-based structure analysis involves imaging thousands or millions of randomly oriented protein molecules fixed in a vitreous ice layer with a uniform thickness of a nanometer scale. The optimal thickness of the vitreous ice should be on the scale of the material of interest in order to minimize inelastic scattering from excess ice. Particularly for imaging low-contrast biological specimens, this optimal condition is important to ensure sufficient signal-to-noise ratios and minimize overlaps of biomolecules along the electron beam path.[10] If the thickness of vitreous ice is too thin, subparts of the structure of biomolecules in the sample can be exposed to the water–air interface during sample preparation, resulting in preferred orientation[11] or local denaturation of the molecules.[12] In addition, the blotting process can cause a loss of about 99% of biomolecules via water soaking by the blotting pad.[13] Due to these difficulties, cryo-EM-based imaging mostly involves extensive manual screening of multiple grids.

Herein, we develop a microfabricated silicon (Si)-chip-based device for straightforward and reliable sample preparation in cryo-EM analysis. The new device has micropatterned holes in a silicon nitride (Si_xN_y) layer with accurately regulated depths to enable precise control of vitreous ice thickness after blotting. Each hole has a window of graphene oxide (GO). The strong affinity of GO for biomolecules is helpful for concentrating the molecules to a higher level in the hole. In addition, the thin but robust Si frame provides a high mechanical stability of the chip during handling in a series of sample preparation procedures and cryo-EM imaging. As a result, the newly developed micropatterned chip with a GO window enables a more straightforward, reliable, and reproducible sample preparation, which can eventually facilitate efficient and high-throughput 3D structure analysis by cryo-EM.

M. K. Ahn, S. M. Lee
Department of Materials Science and Engineering
Seoul National University
Seoul 08826, Republic of Korea

M. K. Ahn, S. M. Lee
Biomedical Implant Convergence Research Lab
Advanced Institutes of Convergence Technology
Suwon 16229, Republic of Korea

B. H. Kim
Department of Organic Materials and Fiber Engineering
Soongsil University
Seoul 06978, Republic of Korea

J. R. Meyerson
Department of Physiology and Biophysics
Weill Cornell Medical College of Cornell University
New York, NY 10065, USA

2. Results and Discussion

The advanced micropatterned chip with a GO window is designed where the depth of the micropatterned Si_xN_y layer is controlled to precisely regulate the thickness of vitreous ice layer depending on the size of the material to be analyzed (**Figure 1**a). Figure 1b shows the fabrication process of the micropatterned chip with a GO window using a microelectromechanical system (MEMS) technique and a 2D nanosheet transfer method. The major advantage of using MEMS fabrication is its facile mass production of Si-based microchips with Si_xN_y windows. For example, about 500 microchips can be produced from one Si wafer with 4 in. diameter from photolithography, dry-etching, and wet-etching processes. The thickness of the Si_xN_y window which will eventually determines the depth of the hole in the micropatterned chips is controlled by a deposition time in a low pressure chemical vapor deposition (LPCVD) process of the Si_xN_y on Si wafer. The LPCVD provides the Si_xN_y layer with a low stress which ensures a high stability of a freestanding Si_xN_y that is tens of nanometers in thickness.[14] Afterward, the micropatterned chip with a GO window is fabricated by applying a lithographic patterning of holes with 2 μm in diameter on the Si_xN_y window. Subsequently, the GO window is constructed by drop casting of GO solution, resulting in a regular array of micrometer-scale well-type structures with GO windows in each microchip. The structure of the micropatterned chip with the GO window is confirmed with an optical microscope (OM) and a scanning electron microscope (SEM), as shown in Figure 1c–f. The micropatterned chip has 100 freestanding Si_xN_y membranes (10×10) with a dimension of 50×20 μm^2. Each freestanding Si_xN_y membrane has tens of microholes having diameters of 2 μm and the GO window. The resulting GO-supported micropatterned chip has ≈10 000 holes, potentially allowing automated large data collection for single particle analysis. Furthermore, since these micropatterned chips are fabricated from the MEMS process, the number and the morphologies of Si_xN_y membranes and GO windowed microholes can be easily manipulated (Figure S1, Supporting Information) for high-throughput single particle analysis and other types of cryo-EM imaging experiment depending on the materials such as viral, cellular, or inorganic materials.

The existence of the thin GO layer across the hole is confirmed by high-resolution transmission electron microscope (HRTEM) images, electron diffraction patterns, and Raman spectrum (**Figure 2**a–d).The HRTEM image of a local region of one GO window (Figure 2a,b) clearly shows a defect-free crystalline GO with measured lattice spacing of 0.25 nm which corresponds to the lattice spacing of GO.[15] The thickness of GO window shown in Figure 2a is measured to be 4 nm (Figure S6f,

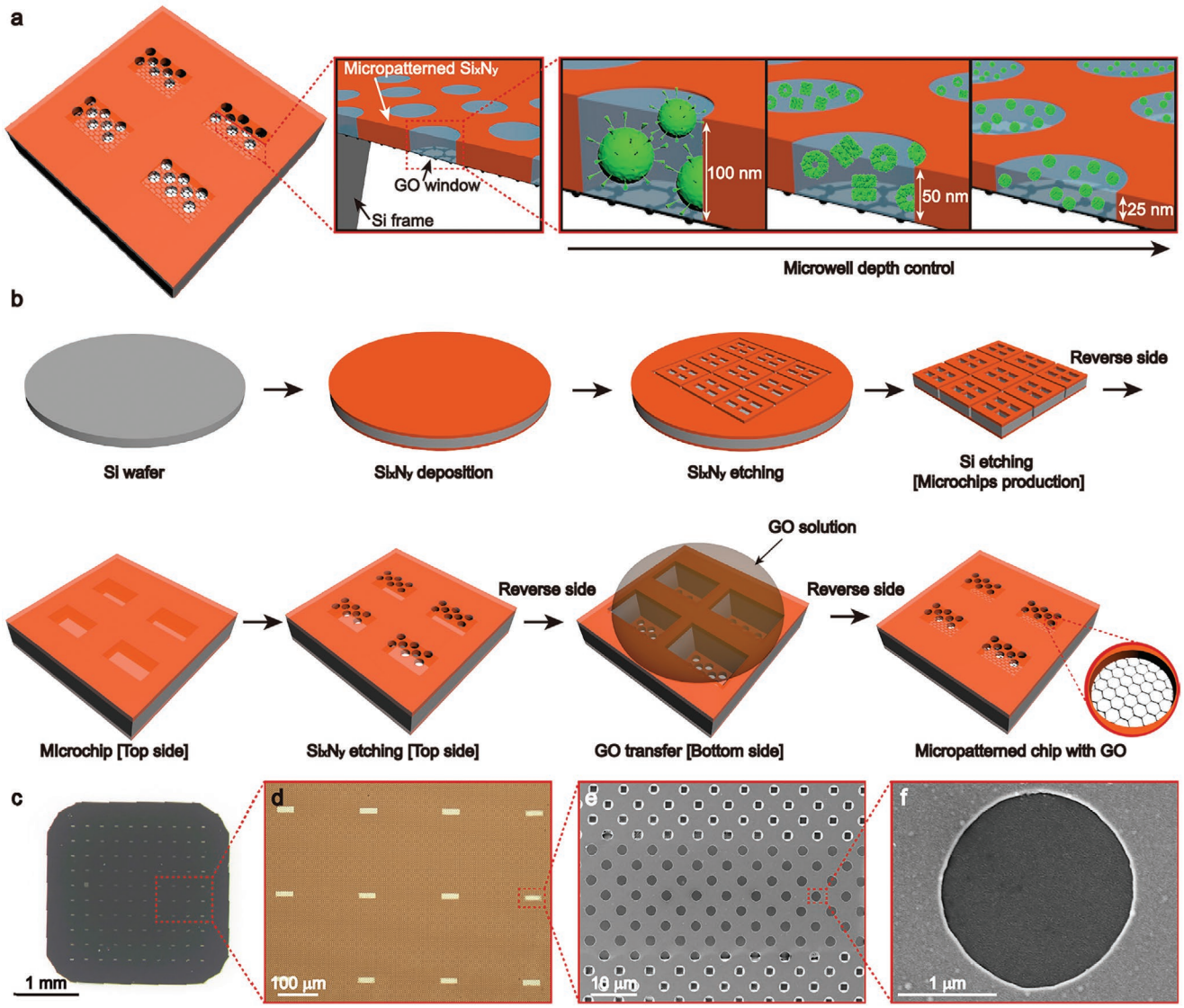

Figure 1. a,b) Schematics of the newly developed micropatterned chip with a GO window for cryo-EM and the fabrication process of the device. Schematics of (a) a cross-section of the device with different depths of micropatterned Si_xN_y regulating the thickness of vitreous ice layer depending on the size of the biomaterials to be observed, and (b) a fabrication process of the micropatterned chip with a GO window. c–f) Structure of the micropatterned chip with a GO window: (c) OM image of a whole micropatterned device, (d) OM image of exposed freestanding Si_xN_y membranes in a device, (e) SEM image of a single micropatterned Si_xN_y membrane, and (f) SEM image of a single microhole with GO window.

Supporting Information) which is ≈10 times thicker than monolayer of graphene,[16] indicating GO multilayers as represented by multiply oriented hexagonal diffraction patterns (Figure 2c). It is noteworthy that the 4 nm thick GO window has no noticeable defect with a uniform contrast throughout the 2 μm hole with minimal impact on TEM resolution,[17] which is an important requirement for efficient cryo-EM imaging. In addition, the thickness of GO window can be regulated by a type of GO transfer method (Supporting Information) and the concentration of GO solution (Figure S2, Supporting Information). Moreover, mono- or bilayer of graphene can be transferred to micropatterned chip with loop-assisted transfer[18] to produce graphene-supported microwell grid (Figure S3, Supporting Information). We also conduct Raman spectroscopy to validate the existence of GO. Raman spectrum at the hole region shows strong D and G bands at 1345 and 1602 cm^{-1}, respectively, with a ratio of I_D/I_G of 0.99. The 1:1 ratio of D and G peaks is a characteristic feature of 2D GO nanosheets.[19] The averaged coverage of GO per micropatterned chip is measured as high as 99.4 ± 0.6% based on SEM observations. This successful preparation of GO window on the micropatterned chip is likely to ensure a high success rate in finding optimal regions for imaging. Furthermore, it potentially enables automated cryo-EM imaging across multiple holes for mass data acquisition because those holes are arranged in a regular pattern.

As explained in the previous paragraph, the GO window can be prepared in the micropatterned chip using different types of transfer methods of GO solution such as drop casting and

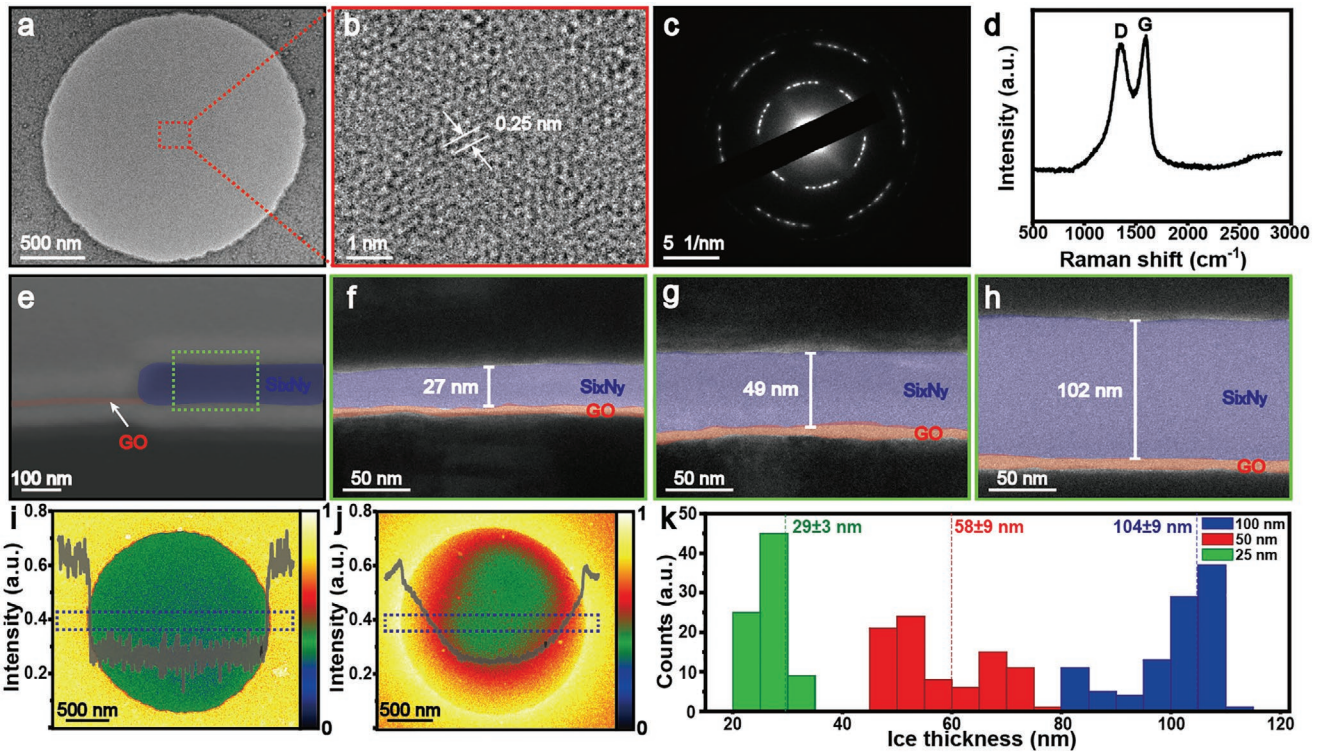

Figure 2. a–d) Confirmation of GO window at the microhole. HRTEM images of (a) a single microhole with a GO window, and (b) the local region of the GO window. (c) Selected area electron diffraction pattern and (d) Raman spectrum of the GO window.e–h) Cross-section morphology of the micropatterned chip with GO window in three representative controlled depths. (e) Cross-sectional SEM image of 100 nm depth micropatterned device. Cross-sectional TEM images of (f) 25 nm, (g) 50 nm, and (h) 100 nm depth micropatterned Si_xN_y layer with a GO window. i–k) Evaluation of vitreous ice layer thickness at micropatterned chip with different depths. EFTEM image and line profile showing the intensity at hole region with vitreous ice of (i) 50 nm depth micropatterned device and (j) conventional holey carbon grid. The linearly normalized intensity scale is shown in the color bar and the dotted rectangular box on EFTEM image indicates the integration width. (k) Histograms of the ice layer thickness in the micropatterned device with different depths (25, 50, and 100 nm). The mean and deviation of ice thicknesses in each device with different depths are indicated with the dotted line and number.

float casting (Supporting Information).[20] A different transfer method of GO can be selected depending on the user's demand. Using a small amount of GO solution, highly flat GO window without noticeable wrinkles can be constructed by drop casting. GO window constructed by drop casting is almost invisible at even high defocus values (Figure 2a) due to its flatness and low background signal. In addition, the drop casting method ensures near 100% coverage of GO over one micropatterned chip. Float casting also forms the GO window with a high hole coverage of ≈99.0% with a benefit of transferring GO to plural devices in one transfer process. The GO solution may penetrate under the device during the float casting transfer procedure, resulting in a relatively thick GO window by GO nanosheets that cover both top and bottom surfaces of the micropatterned Si_xN_y (Figure S5a–d, Supporting Information). If needed, this can be avoided by mounting and sealing an array of micropatterned chips onto a rigid substrate for dispensing the GO solution (Figures S4 and S5e–h, Supporting Information).

We demonstrate the capability of regulating the depth of microholes by fabricating micropatterned Si_xN_y chips with GO window in three representative target depths: 25, 50, and 100 nm. To evaluate the morphology and the thickness of the micropatterned Si_xN_y with GO window, cross-sections of devices obtained from focused ion beam (FIB) sectioning are observed with SEM and TEM (Figure 2e–h and Figure S6d,e (Supporting Information)). Well-type structure of the microhole with GO window is clearly shown in the SEM image (Figure 2e). Thicknesses of Si_xN_y are measured to be 28 ± 2, 48 ± 2, and 103 ± 1 nm, confirming both successful control of the depth of the Si_xN_y microhole and the transfer of the GO window.

Vitreous ice with a uniform and precise thickness can be formed using the micropatterned device with controlled depth. The relative thickness of vitreous ice formed at a single microhole of micropatterned device is evaluated with energy-filtered TEM (EFTEM). The detected intensity which is related to the relative thickness of the material is displayed with a color map and line profile, confirming uniform thickness of vitreous ice throughout the microhole region (Figure 2i). On the contrary, cryosamples prepared using conventional holey carbon grid had irregular thickness of the vitreous ice at the hole region, showing a thick ice layer at the edge of the hole and thin ice layer at the center of the hole (Figure 2j) which are resulted from surface tension of the solution with a large portion of exposed water–air interface.[21] GO membrane at micropatterned device reduces the exposed water–air interface, enhancing the ice thickness uniformity. The uniform ice layer at a single microhole provides a similar degree of defocusing parameter which allows an efficient and reliable downstream

image processing for 3D reconstruction of a biomolecule structure. In addition, the thickness of vitreous ice is investigated by integration of electron energy loss spectrum (EELS).[22] Representative EELS spectra of the vitreous ice layer formed in the hole of micropatterned chip with different depths (25, 50, and 100 nm) are shown in Figure S9 (Supporting Information). As the depth of the micropatterned Si_xN_y increases from 25 to 100 nm, scanned peak intensity from 1 to 30 eV increases, confirming that the ice layer becomes thicker. Using the following equation

$$d = \lambda \ln \frac{I}{I_{zlp}} \tag{1}$$

where d is the vitreous ice thickness, λ is the mean free path of inelastic scattering (287 nm in TEM with accelerating voltage of 200 keV),[23] I is the integrated total intensity, and I_{zlp} is the integrated zero-loss peak intensity, the thickness of the vitreous ice can be calculated. The measurement of the thickness of vitreous ice based on EELS mapping is repeated throughout multiple holes in the micropatterned chip (Figure 2k). The average ice thicknesses formed inside the micropatterned chips with depths of 25, 50, or 100 nm are 29 ± 3, 58 ± 9, or 104 ± 9 nm, respectively, showing that the depth of the microholes can determine the thickness of the vitreous ice. In all three types of devices with different depths, the thickness of the vitreous ice is uniform throughout multiple holes in the device, as indicated by the narrow distribution in the histograms for the measured thickness of the vitreous ice. Thick vitreous ice layer can reduce the signal of biomolecules due to the enhanced background scattering of electron beam.[24] This highlights the importance of the controlled thicknesses of the vitreous ice in the cryo-EM imaging depending on the size of the biological molecules. The depth controllability of the micropatterned device can facilitate efficient structural analysis by making optimal thickness of ice for proteins of interest.

Since organic, biological, and inorganic materials have different sizes, formation of vitreous ice with an appropriate thickness can ensure enhanced contrast resolution with minimized structure perturbation of the sample molecules during cryo-EM imaging. To demonstrate the biological application and compatibility with high-resolution cryo-EM, we prepare frozen hydrated grid chips with human immunodeficiency virus (HIV-1, ≈100 nm size), apoferritin (470 kDa), and aldolase (157 kDa) using 100, 50, and 25 nm depth micropatterned chips and GO window, respectively. HIV-1 is a representative pathogenic virus that has caused more than 30 million of deaths, and around 40 million people carry the virus today.[25] Viruses, self-assembled nanoscale complexes, are composed of proteins and nucleic acids. Many enveloped viruses additionally contain lipid molecules in their surface. Apoferritin are standard proteins which are customarily used for benchmarking workflows and methods in cryo-EM structure analysis.[26] Each chip is then assembled into an autogrid and transferred to 200 keV Glacios equipped with Falcon 4 direct electron camera. Cryo-EM movie is collected using 35–40 e^- $Å^{-2}$ dose for each specimen and drift-corrected microscopy images displayed clear particles with high frequency thorn rings in fast Fourier transform extending close to Nyquist signal (**Figure 3**a–c and Figures S11 and S12a (Supporting Information)). Cryo-EM image of a spherical HIV-1 particles displaying foreign envelope proteins, vesicular stomatitis virus glycoproteins, is obtained using the 100 nm depth micropatterned devices (Figure 3a). In addition, apoferritin protein is imaged by cryo-EM using the 50 nm depth micropatterned chip (Figure 3b). We also demonstrate that smaller-sized proteins such as aldolase are clearly observed using 25 nm depth micropatterned chip, as shown in Figure 3c. Furthermore, we also obtain cryo-EM images of aldolase from micropatterned chips with 50 and 100 nm depths. Aldolase is clearly observed from 50 and 100 nm depth micropatterned device (Figure S11, Supporting Information). We perform a session for automated data collection on apoferritin using manufacturer provided software (EPU). Automated functions including grid navigation, autofocus, hole selection, and image acquisition are performed well on the chip. In particular, we can take advantage of regular arrangements of microfabricated 2 μm diameter hole of the chip for multi-exposure per hole and the fast mode imaging of EPU as well, allowing high throughput data collection on a 200 keV microscope. Apoferritin particles are well converged and the 3D structure is reconstructed at 3.06 Å resolution (Figure 3d,e). The density map of apoferritin shows clear side chains of helices and loops. It also shows its resolution of near 2.7 Å, which can be confirmed through the local resolution map. While the physical Nyquist frequency is ≈2.7 Å in these images, a diffraction pattern of GO (≈2.1 Å) is visible in the Fourier transformed image with 2 × 2 supersampling of microscopy images (Figure S12a, Supporting Information). Taken together, our experiment indicates that the chip is compatible with high-end cryo-EM instruments and suitable for the near-atomic structural study.

Our newly developed devices provide an important capability for cryo-EM imaging of several biological entities including proteins and complexes of lipids, proteins, and nucleic acids. Affinity of GO surface to biomolecules can lead to concentration of the molecules within the electron-beam transparent area during solution loading (**Figure 4**a–c). We count the number of biological entities (HIV-1 and groEL) captured in the GO window of the micropatterned chip and compare it with the one obtained using the a conventional holey carbon grid. The number density of HIV-1 particles within the GO windows of the microchip is 2 μm^{-2}, whereas that within the hole of holey carbon grid is only 1 μm^{-2} (Figure 4a,c). Such difference is also consistently observed during cryo-EM imaging of groEL protein molecules. About 950 proteins are concentrated in a unit area (1 μm^2) of GO holes of microchips during sample preparations but only about 490 proteins μm^{-2} is detected in a commercial cryo-EM grid (Figure 4b,c). In addition, tomography is conducted at the GO-supported microwell grid with apoferritin to investigate the distribution of the protein particles inside the vitreous ice layer. Protein particles are observed to distribute in monolayer close to the GO layer (Figure S13 and Movie S1, Supporting Information).[27] Concentrating biomolecules in the imaging area of a micropatterned device can potentially enhance the efficiency of the downstream image process for sample molecule structure construction because it reduces the required number of images and the imaging time. Furthermore, the use of the micropatterned chip with a GO window

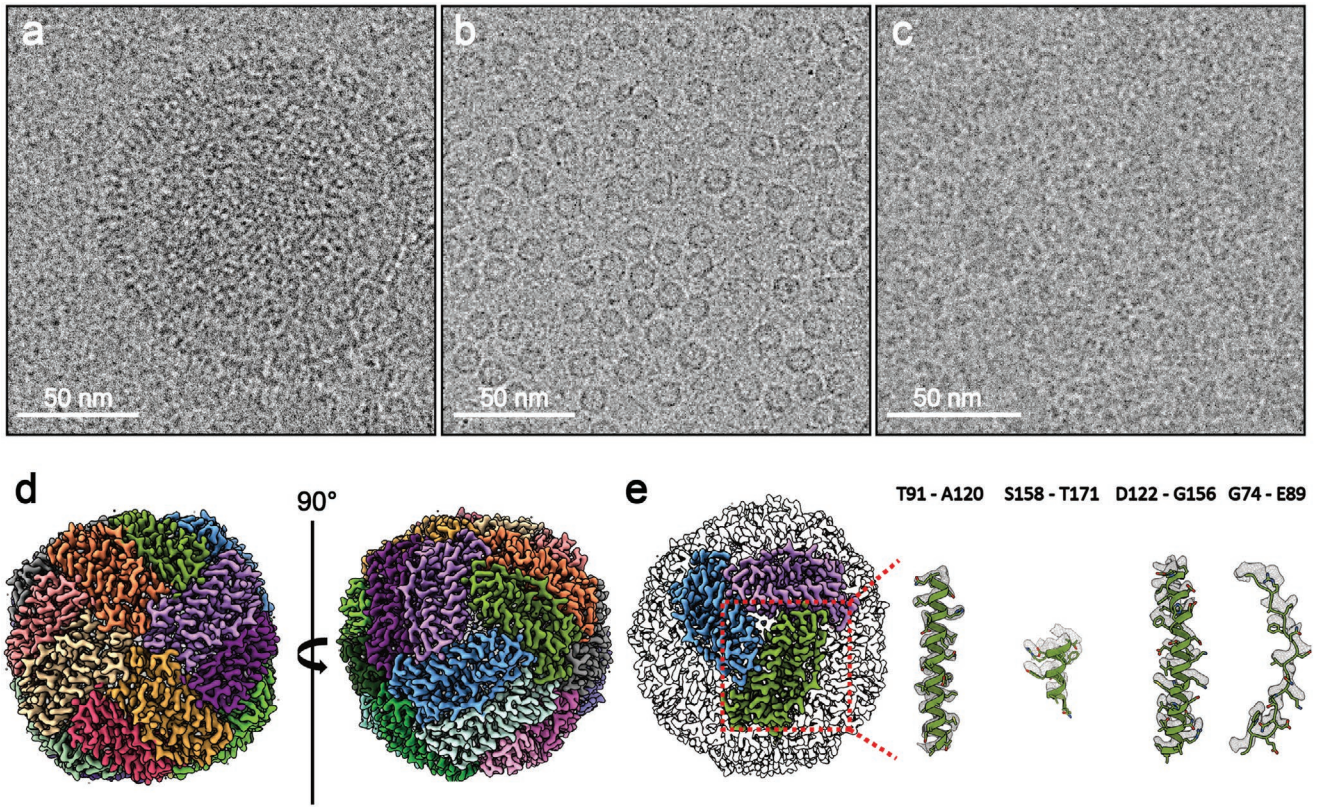

Figure 3. a–c) Cryo-EM images of various sized biomaterials in different depths of micropatterned chip. (a) HIV-1 (≈100 nm size) in 100 nm, (b) apoferritin protein (470 kDa) in 50 nm, and (c) aldolase protein (157 kDa) in 25 nm depth micropatterned device. d) 3.06 Å Cryo-EM map of horse apoferritin and e) the fitted helices model (6RJH) and the corresponding density.

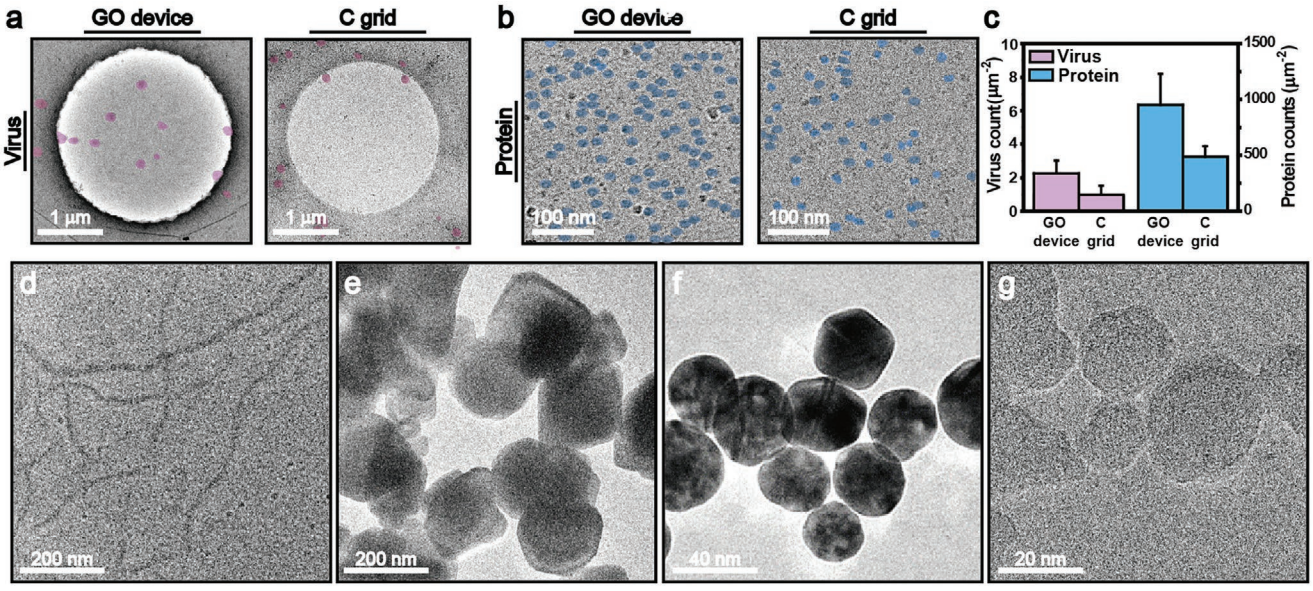

Figure 4. a–c) Comparison of biomaterial concentration observed with micropatterned chip with GO window and conventional holey carbon grid. Cryo-EM images of (a) HIV-1 virus with 100 nm depth GO device and carbon grid, respectively, and (b) groEL protein with 50 nm depth GO device and carbon grid, respectively, and (c) concentration of the biomaterials observed in GO device and carbon grid at the microhole region. d–g) Cryo-EM images of various materials with the micropatterned device. (d) Tau protein with tubular structure, and (e) Fe_2O_3 nanoparticle in 100 nm, (f) Au nanoparticle in 50 nm, and (g) silica in 25 nm depth micropatterned chip, respectively.

requires a small amount of biomolecules and mitigates the denaturation that occurs at the air–water interface.

Besides single molecular particles of biomolecules, diverse types of materials are also observed by the micropatterned chip with GO window based on the choice of different depth depending on the size of the material. We demonstrate several examples. Tau proteins fibrillized with heparin are visualized by cryo-EM with a 100 nm depth microchip. Its fibrillar morphology and width (≈10 nm) are virtually identical to those observed from conventional cryo-EM but exhibited more twisted contour (Figure 4d). Inorganic materials such as Fe_2O_3 nanoparticles, Au nanoparticles, and silica nanoparticles are also investigated using 100, 50, and 25 nm depth micropatterned devices, respectively (Figure 4e–g and Figure S14 (Supporting Information)).

3. Conclusion

A micropatterned chip with a GO window is fabricated by the MEMS technique with transfer of 2D GO nanosheets. The well-type structure of microhole with a GO window is constructed with controlled depths from 25 to 100 nm, enabling fine thickness control of vitreous ice in sample preparation for cryo-EM. Moreover, the high affinity of GO for biomolecules concentrates sample molecules at a higher level on the electron-transparent hole region. Cryo-EM using such micropatterned chips is efficient, as demonstrated by successful imaging of multimeric protein complex, such as HIV-1, groEL, apoferritin, aldolase, and fibrillized tau protein. Furthermore, micropatterned chip shows compatibility with high-end cryo-EM instruments and feasibility for the near-atomic single particle analysis. Our device and the method can also be applied to cryoimaging of inorganic materials. As a result, the newly developed micropatterned chip with GO window enables a more straightforward, reliable, and reproducible sample preparation strategy that can eventually facilitate efficient and high-throughput 3D structure analysis with cryo-EM.

4. Experimental Section

The detailed experimental process is available in the Supporting Information.

Supporting Information

Supporting Information is available from the Wiley Online Library or from the author.

Acknowledgements

M.-H.K. and J.P. contributed equally to this work. M.-H.K., S.K., M.L., and J.P. acknowledge the financial support from the Institute for Basic Science (Grant No. IBS-R006-D1). S.K., M.L., and J.P. acknowledge the financial support from Creative-Pioneering Researchers Program through Seoul National University (2020) and the NRF grant funded by the Korean government (MSIT; Grant Nos. NRF-2020R1A2C2101871, NRF-2021M3A9I4022965 and NRF-2021M3H4A1A02045989). M.L. and J.P. acknowledge the financial support from the POSCO Science Fellowship of POSCO TJ Park Foundation and the NRF grant funded by the Korean government (MSIT; Grant No. NRF-2017R1A5A1015365). J.P. acknowledges the financial support from the Agency for Defense Development (ADD, Grant No. UC190025RD). J.P. and S.-H.R. acknowledge the financial support from the NRF grant funded by the Korean government (MSIT; Grant No. NRF-2020R1A6C101A183). S.-H.R. acknowledges the financial support from Creative-Pioneering Researchers Program through Seoul National University and the NRF grant funded by the Korean government (MSIT; Grant Nos. NRF-2019M3E5D6063871, 2019R1C1C1004598, and 2020R1A5A1018081). M.J.L. and J.P. acknowledge the financial support from the Interdisciplinary Research Initiatives Programs by College of Engineering and College of Medicine, Seoul National University (2021). M.-H.K. acknowledges the financial support from the NRF grant funded by the Korean government (MSIT; Grant No. NRF-2020R1I1A1A0107416612). B.H.K. acknowledges the financial support from NRF grant funded by the Korean government (MSIT; Grant No. NRF-2021R1C1C1014339). K.-I.L. acknowledges the financial support from the NRF grant funded by the Korean government (MSIT; Grant No. NRF-2020R1A2C2005893). S.J. and W.C.L. acknowledge the support from the NRF of Korea funded by the MSIT (Grant No. 2021R1A2C1011797). The authors thank the staff and crew of the National Center for Inter-University Research Facility (NCIRF) for their untiring efforts and perseverance with the TEM experiments.

Conflict of Interest

The authors declare no conflict of interest.

Data Availability Statement

Data available on request due to privacy/ethical restrictions.

Keywords

cryogenic-electron microscope, graphene oxide, microelectromechanical systems, nanomaterials, vitreous ice thickness

Received: April 20, 2021
Revised: August 11, 2021
Published online:

[1] a) R. S. Dillard, C. M. Hampton, J. D. Strauss, Z. L. Ke, D. Altomara, R. C. Guerrero-Ferreira, G. Kiss, E. R. Wright, *Microsc. Microanal.* **2018**, *24*, 406; b) B. J. Xu, L. Liu, *Protein Sci.* **2020**, *29*, 872; c) K. Murata, M. Wolf, *Biochim. Biophys. Acta, Gen. Subj.* **2018**, *1862*, 324; d) P. L. Stewart, *Wiley Interdiscip. Rev.: Nanomed. Nanobiotechnol.* **2017**, *9*, e1417; e) A. A. Kermani, *FEBS J.* **2020**, https://doi.org/10.1111/febs.15676.

[2] J. P. Renaud, A. Chari, C. Ciferri, W. T. Liu, H. W. Remigy, H. Stark, C. Wiesmann, *Nat. Rev. Drug Discovery* **2018**, *17*, 471.

[3] a) R. Fernandez-Leiro, S. H. W. Scheres, *Nature* **2016**, *537*, 339; b) H. Elmlund, D. Elmlund, S. Bengio, *Structure* **2013**, *21*, 1299; c) P. D. B. Olinares, J. Y. Kang, E. Llewellyn, C. Chiu, J. Chen, B. Malone, R. M. Saecker, E. A. Campbell, S. A. Darst, B. T. Chait, *Structure* **2021**, *29*, 186.

[4] a) K. Naydenova, P. P. Jia, C. J. Russo, *Science* **2020**, *370*, 223; b) L. A. Passmore, C. J. Russo, *The Resolution Revolution: Recent Advances in CryoEM*, (Ed: R. A. Crowther), Methods in Enzymology, Vol. *579*, Elsevier, Amsterdam **2016**, p. 51.

[5] a) Y. Zhang, B. F. Sun, D. Feng, H. L. Hu, M. Chu, Q. H. Qu, J. T. Tarrasch, S. Li, T. S. Kobilka, B. K. Kobilka, G. Skiniotis, *Nature* **2017**, *546*, 248; b) Y. F. Cheng, *Curr. Opin. Struct. Biol.* **2018**, *52*, 58.
[6] a) C. Liu, L. Mendonca, Y. Yang, Y. Z. Gao, C. G. Shen, J. W. Liu, T. Ni, B. Ju, C. C. Liu, X. Tang, J. L. Wei, X. M. Ma, Y. N. Zhu, W. L. Liu, S. M. Xu, Y. X. Liu, J. Yuan, J. Wu, Z. Liu, Z. Zhang, L. Liu, P. Y. Wang, P. J. Zhang, *Structure* **2020**, *28*, 1218; b) M. M. Shaik, H. Q. Peng, J. M. Lu, S. Rits-Volloch, C. Xu, M. F. Liao, B. Chen, *Nature* **2019**, *565*, 318; c) M. Hauser, W. J. Dearnaley, A. C. Varano, M. Casasanta, S. M. McDonald, D. F. Kelly, *Comput. Struct. Biotechnol. J.* **2019**, *17*, 1178.
[7] S. R. Spurgeon, C. Ophus, L. Jones, A. Petford-Long, S. V. Kalinin, M. J. Olszta, R. E. Dunin-Borkowski, N. Salmon, K. Hattar, W. C. D. Yang, R. Sharma, Y. G. Du, A. Chiaramonti, H. M. Zheng, E. C. Buck, L. Kovarik, R. L. Penn, D. S. Li, X. Zhang, M. Murayama, M. L. Taheri, *Nat. Mater.* **2021**, *20*, 274.
[8] a) Y. Z. Li, Y. B. Li, A. L. Pei, K. Yan, Y. M. Sun, C. L. Wu, L. M. Joubert, R. Chin, A. L. Koh, Y. Yu, J. Perrino, B. Butz, S. Chu, Y. Cui, *Science* **2017**, *358*, 506; b) X. C. Ren, X. Q. Zhang, R. Xu, J. Q. Huang, Q. Zhang, *Adv. Mater.* **2020**, *32*, 1908293; c) Y. B. Li, W. Huang, Y. Z. Li, W. Chiu, Y. Cui, *ACS Nano* **2020**, *14*, 9263; d) J. Y. Wang, W. Huang, A. Pei, Y. Z. Li, F. F. Shi, X. Y. Yu, Y. Cui, *Nat. Energy* **2019**, *4*, 664; e) U. M. Mirsaidov, H. M. Zheng, Y. Casana, P. Matsudaira, *Biophys. J.* **2012**, *102*, L15.
[9] a) N. A. Alden, A. C. Varano, W. J. Dearnaley, M. J. Solares, W. Y. Luqiu, Y. P. Liang, Z. Sheng, S. M. McDonald, J. Damiano, J. McConnell, M. J. Dukes, D. F. Kelly, *Small* **2019**, *15*, e1900918; b) J. R. Meyerson, P. Rao, J. Kumar, S. Chittori, S. Banerjee, J. Pierson, M. L. Mayer, S. Subramaniam, *Sci. Rep.* **2014**, *4*, 7084.
[10] W. J. Rice, A. C. Cheng, A. J. Noble, E. T. Eng, L. Y. Kim, B. Carragher, C. S. Potter, *J. Struct. Biol.* **2018**, *204*, 38.
[11] J. Chen, A. J. Noble, J. Y. Kang, S. A. Darst, *J. Struct. Biol.: X* **2019**, *1*, 100005.
[12] D. Elmlund, H. Elmlund, *Annu. Rev. Biochem.* **2015**, *84*, 499.
[13] a) R. M. Glaeser, *Nat. Methods* **2016**, *13*, 28; b) D. Elmlund, S. N. Le, H. Elmlund, *Curr. Opin. Struct. Biol.* **2017**, *46*, 1.
[14] a) C. Yang, J. Pham, *Silicon* **2018**, *10*, 2561; b) J. M. Olson, *Mater. Sci. Semicond. Process.* **2002**, *5*, 51; c) B. R. Zheng, C. Zhou, Q. Wang, Y. F. Chen, W. Xue, *Adv. Mater. Sci. Eng.* **2013**, *2013*, 835942; d) W. H. Chuang, R. K. Fettig, R. Ghodssi, *Sens. Actuators, A* **2005**, *121*, 557; e) J. H. Kim, Q. Zhou, J. Y. Chang, *Micromachines* **2017**, *8*, 44.
[15] C. Gomez-Navarro, J. C. Meyer, R. S. Sundaram, A. Chuvilin, S. Kurasch, M. Burghard, K. Kern, U. Kaiser, *Nano Lett.* **2010**, *10*, 1144.
[16] Z. H. Ni, H. M. Wang, J. Kasim, H. M. Fan, T. Yu, Y. H. Wu, Y. P. Feng, Z. X. Shen, *Nano Lett.* **2007**, *7*, 2758.
[17] J. M. Yuk, Q. Zhou, J. Y. Chang, P. Ercius, A. P. Alivisatos, A. Zettl, *ACS Nano* **2016**, *10*, 88.
[18] P. M. G. van Deursen, R. I. Koning, V. Tudor, M.-A. Moradi, J. P. Patterson, A. Kros, N. A. J. M. Sommerdijk, A. J. Koster, G. F. Schneider, *Adv. Funct. Mater.* **2020**, *30*, 1904468.
[19] a) F. T. Johra, J. W. Lee, W. G. Jung, *J. Ind. Eng. Chem.* **2014**, *20*, 2883; b) S. M. Hafiz, R. Ritikos, T. J. Whitcher, N. M. Razib, D. C. S. Bien, N. Chanlek, H. Nakajima, T. Saisopa, P. Songsiriritthigul, N. M. Huang, S. A. Rahman, *Sens. Actuators, B* **2014**, *193*, 692.
[20] E. Palovcak, F. Wang, S. Q. Zheng, Z. L. Yu, S. Li, M. Betegon, D. Bulkley, D. A. Agard, Y. F. Cheng, *J. Struct. Biol.* **2018**, *204*, 80.
[21] A. J. Noble, V. P. Dandey, H. Wei, J. Braschi, J. Chase, P. Acharya, Y. Z. Tan, Z. N. Zhang, L. Y. Kim, G. Scapin, M. Rapp, E. T. Eng, W. J. Rice, A. C. Cheng, C. J. Negro, L. Shapiro, P. D. Kwong, D. Jeruzalmi, A. des Georges, C. S. Potter, B. Carragher, *Elife* **2018**, *7*, e34257.
[22] H.-J. Cho, J.-K. Hyun, J.-G. Kim, H. S. Jeong, H. N. Park, D.-J. You, H. S. Jung, *J. Anal. Sci. Technol.* **2013**, *4*, 7.
[23] a) K. Lim, Y. Bae, S. Jeon, K. Kim, B. H. Kim, J. Kim, S. Kang, T. Heo, J. Park, W. C. Lee, *Adv. Mater.* **2020**, *32*, 2002889; b) B. Feja, U. Aebi, *J. Microsc.* **1999**, *193*, 15.
[24] S. P. Wu, J. P. Armache, Y. F. Cheng, *Microscopy* **2016**, *65*, 35.
[25] UNAIDS Data 2020, https://www.unaids.org/en/resources/fact-sheet (accessed: 2021).
[26] R. B. G. Ravelli, F. J. T. Nijpels, R. J. M. Henderikx, G. Weissenberger, S. Thewessem, A. Gijsbers, B. W. A. M. M. Beulen, C. Lopez-Iglesias, P. J. Peters, *Nat. Commun.* **2020**, *11*, 2563.
[27] E. D'Imprima, D. Floris, M. Joppe, R. Sanchez, M. Grininger, W. Kuhlbrandt, *Elife* **2019**, *8*, e42747.